# Automatic band selection for wavelet reconstruction in the application of defect detection

D. M. Tsai and C. H. Chiang
Machine Vision Lab.
Department of Industrial Engineering and Management
Yuan-Ze University, Chung-Li, Taiwan, R.O.C.
E-mail: iedmtsai@saturn.yzu.edu.tw

## ABSTRACT

In this paper, we present a multiresolution approach for the inspection of local defects embedded in homogeneously textured surfaces. It is based on an efficient image restoration scheme using the wavelet transforms. By properly selecting the smooth subimage or the combination of detail subimages at different resolution levels for image reconstruction, the global repetitive texture pattern can be effectively removed and only local anomalies are preserved in the restored image. A wavelet band selection procedure is developed to automatically determine the best reconstruction parameters based on the energy distribution of wavelet coefficients. Experimental results show that the decomposed subimages and the number of resolution levels determined by the automatic band selection scheme are similar to the manual selection results, and the defects in a variety of real textures including machined surfaces, natural wood, sandpaper and textile fabrics are well detected.

*Keywords*: Surface inspection, Defect detection, Textured image, Wavelet transform,
Band selection

# 1. INTRODUCTION

Image analysis techniques are being increasingly used to automate the detection of defects in complicated material surfaces. In this study, we propose a wavelet reconstruction scheme for automatic surface inspection. In automatic surface inspection, one has to solve the problem of detecting small surface defects that locally break the homogeneity of a texture pattern. Most of the defect detection algorithms tackle the problem by extracting a set of textural features using co-occurrence matrix approaches, the Fourier transform, the Gabor transform and the wavelet transform. Co-occurrence matrix methods have been a popular spatial domain approach for texture analysis. A survey of co-occurrence matrix methods can be found in Siew and Hodgson [1]. They were applied to the inspection of wood [2], and machined-surface roughness [3].

Fourier-based methods characterize the spatial-frequency distribution of textured images, but they do not consider the information in the spatial domain and may ignore local deviations. Liu and Jernigan [4] reviewed a set of 28 textural features extracted from the Fourier spectra. The reported applications of spatial-frequency methods in texture analysis are mainly limited to texture classification and segmentation [5-7]. Gabor filters [8] have been well recognized as a joint spatial/spatial-frequency representation for analyzing textured images that contain highly specific frequency and orientation characteristics. Gabor-filter based methods were successfully applied to texture segmentation [9-12], and inspection [13, 14]. Gabor filtering methods are very computational expensive since the 2D convolution between the image and filter must be carried out in a sliding window throughout the entire image. In addition, the design of optimal

Gabor filters [15, 16] is a very complicated task. Human intervention is generally required to assist in selecting the best filter parameter values of orientation, frequency and Gaussian scale.

In the recent past, wavelet transforms have been a popular alternative for the extraction of textural features. The 2D wavelet transform was defined by Lemarie and Meyer [17], and the use of wavelets for texture analysis was pioneered by Mallat [18]. Textural features extracted from wavelet-decomposed images were widely used for texture classification and segmentation [19-21]. Lambert and Bock [22] derived a feature vector from the coefficients of wavelet packet decomposition. Neural network and Bayes classifiers are then used to evaluate the feature vector for texture defect detection. Amet *et al*. [23] presented a defect detection algorithm based on the wavelet decomposition of images. Statistical features are extracted from the subband images using co-occurrence matrix techniques.

Song *et al*. [24] surveyed texture defect detection methods in global and local categories. Song *et al*. [25, 26] studied surface inspection on random macro textures and, in particular, marble and granite surfaces that contain highly irregular textures. They proposed a two-stage chromatic-structural approach. The first stage uses a histogram-based color clustering scheme to segment a color image into different color classes. The second stage then extracts structural features by blob analysis from each chromatic class separated in the first stage. The Bayes classifier and the Mahalanobis distance are respectively applied to identify color and blob defects.

The texture analysis methods aforementioned are generally based on the extraction of textural features in the spatial and spectral domains. Textures that are characterized by a vector of multiple features result in high dimensionality. This calls for sophisticated classifiers such as Bayes [27], maximum likelihood [28], and neural network [29] to discriminate textural variations. Besides high-dimensional feature spaces, the most difficult task of the feature-extraction approach is to choose adequate textural features which can sufficiently represent the uniqueness of the texture in the image. A set of features that is an optimal representation of a specific texture could be completely useless for other texture patterns.

In this paper, we propose an image reconstruction approach based on the analysis and synthesis wavelet transforms for inspecting surface defects embedded in homogeneous structural and statistical textures. It does not rely on textural features to detect local anomalies, and alleviates all limitations of feature-extraction methods. For one level of standard wavelet decomposition, we obtain one smooth subimage which is a coarse approximation of the original image, and three detail subimages which contain fine structures in horizontal, vertical and diagonal orientations. With proper selection of a smooth subimage or the combination of detail subimages at different multiresolution levels for image reconstruction, the global repetitive texture pattern can be effectively removed and only local anomalies are preserved in the restored image. A simple binary thresholding is therefore used to separate the defective regions from the uniform gray-level background in the restored image. The efficacy of the wavelet reconstruction scheme depends on the number of resolution levels and the decomposed subimages selected for reconstruction. In this study, we develop a wavelet band selection procedure that can automatically determine the number of resolution levels and decomposed subimages for the best discrimination of defects and removals of repetitive texture patterns in the image. This eliminates human intervention for the choice of best reconstruction parameters. The selection criteria for image reconstruction are based on the energy distributions of the wavelet coefficients in all decomposed subimages at different multiresolution levels.

This paper is organized as follows: Section 2 first discusses briefly the effect of varied wavelet band selections on image reconstruction for both structural and statistical textures. The energy distributions of wavelet coefficients derived from the wavelet decomposition are then discussed for the choice of the number of resolution levels and the decomposed subimages. Section 3 presents the experimental results from a variety of structural and statistical textures. This paper is concluded in Section 4.

## 2. WAVELET RECONSTRUCTION AND ENERGY DISTRIBUTIONS

### 2.1 The Effect of Band Selection on Image Reconstruction

Let $f(x,y)$ be the input image of size $M \times N$. One level of wavelet decomposition on $f(x,y)$ results in four subimages: one smooth subimages $f_{LL}(x^{'},y^{'})$, which represents the coarse approximation of the image, and three detail subimages $f_{LH}(x^{'},y^{'})$, $f_{HL}(x^{'},y^{'})$, and $f_{HH}(x^{'},y^{'})$, which represent the horizontal, vertical, and diagonal directions of the image, respectively. Further, let $f_{LL}^{(j)}(x,y)$ represent the smooth subimage at resolution level $j$, and $f_{LL}^{(0)}(x,y) = f(x,y)$, which is the original image. Then the decomposition of $f_{LL}^{(j)}(x,y)$ results in four subimages $f_{LL}^{(j+1)}(x^{'},y^{'})$, $f_{LH}^{(j+1)}(x^{'},y^{'})$, $f_{HL}^{(j+1)}(x^{'},y^{'})$, and $f_{HH}^{(j+1)}(x', y')$ at resolution level $j+1$, each of size $\frac{M}{2^{j+1}} \times \frac{N}{2^{j+1}}$. The pyramid decomposition algorithm for $f_{LL}^{(j)}(x, y)$, $f_{LH}^{(j)}(x, y)$, $f_{HL}^{(j)}(x, y)$ and $f_{HH}^{(j)}(x, y)$ can be found in reference [18].

The inverse 2D wavelet transform for image reconstruction can be also implemented using a backward 2D pyramid algorithm [18]. In the application of wavelet reconstruction for defect detection, we do not want to perfectly restore the textured image. Rather, our goal is to eliminate all regular, repetitive texture patterns in the restored image by selecting proper smooth or detail subimages for wavelet synthesis. Let $W^{-1}[f^{(j)}]$ denote the iteration of the inverse wavelet transform of a subimage $f^{(j)}$ from resolution level $j$ to level 0 (the level with the original image size $M \times N$). The restored image shown in Figure 1(b) is the result of reconstructing the smooth subimage at resolution level 3, i.e., $W^{-1}[f_{LL}^{(3)}]$, for the sandpaper texture shown in Figure 1(a). Figure 2(d) is obtained from the reconstruction of the horizontal and diagonal detail subimages at resolution level 1, i.e., $W^{-1}[f_{LH}^{(1)}] + W^{-1}[f_{HH}^{(1)}]$ for the oriented texture shown in Figure 2(a).

For statistical textures with isotropic patterns, only the smooth subimage needs to be included in the reconstruction process to enhance the defects in the restored image. Figures 1(d) and 1(e) demonstrate that reconstructing detail subimages cannot enhance the defect in the restored image, and no defect is detected in the corresponding binary image. Reconstructing the smooth subimage can effectively highlight the defective regions in the restored image. It well separates defects from the background in the corresponding binary image, as shown in Figures 1(b) and 1 (c).

For structural textures with high directionality, the selective detail subimages, which have different direction emphasis from the original oriented pattern, are included in the reconstruction process to remove all repetitive, oriented textures. Figures 2(d) and 2(e) demonstrate that the restoration from the horizontal and diagonal detail subimages can effectively remove all repetitive vertical-line patterns, and preserve only the local anomaly. However, residuals of repetitive lines remain in the restored image if the smooth subimage is selected for reconstruction, as seen in Figures 2(b) and 2(c).

Too large the number of multiresolution levels causes the fusion effect of defects in the restored image, whereas too small the number of multiresolution levels cannot sufficiently separate defective regions from the homogeneous texture region. The effect of varying number of multiresolution levels on restoration results for a sandpaper texture is demonstrated in Figure 3.

In our empirical study, we found that orthogonal wavelets generally outperform biorthogonal wavelets since biorthogonal wavelets lack of orthogonality properties. The choice of orthogonal wavelet bases has only small effects on the detection results. However, the longer supports of a wavelet basis may oversmooth the local anomalies, and are less computationally efficient. A shortest support of 2 such as the Haar wavelet performs poorly and yields the block effect in the restored image. Throughout this paper, the 8-tap Symmlets (S8) [30] is used for wavelet analysis and synthesis.

## 2.2 Automatic Selection of Decomposed Subimages

In this study, we have considered two types of textures: statistical textures with isotropic patterns such as sandpaper, and structural textures with oriented patterns such as machined surfaces. Image reconstruction for isotropic patterns is obtained from the smooth subimage, whereas image reconstruction for oriented patterns is obtained from selective detail subimage(s). Discrimination between isotropic and oriented patterns can be achieved by comparing the energy magnitude in each decomposed subimage. For isotropic patterns, the energy responses in high frequency subbands (detail subimages) are not significant. The energy values in the horizontal, vertical and diagonal detail subimages are approximately equally distributed. The main energy is concentrated on the low frequency subband (smooth subimage). The energy response of the smooth subimage of an isotropic texture is distinctly larger than that of an oriented texture. For structural textures with specific directional line patterns, the detail subimages that correspond to the line directions in the original image have significantly larger energy values than the ones that contain no directional information of the original image. For instance, given a machined surface with vertical feedmarks in the image, the vertical detail subimage has distinctly larger energy value, compared to the horizontal and diagonal subimages which have energy values close to zero.

In this study, we use the $l_2$-norm as the energy function to identify dominant frequency subbands of a textured pattern. Let $J$ be the total number of decomposition levels. The energy of each decomposed subimage is calculated as follows:

The energy of the smooth subimage at level $J$ is given by

$$E_s^J = \sum_x \sum_y [f_{LL}^{(J)}(x,y)]^2 \tag{1a}$$

The energy of the horizontal detail subimage at level $j$:

$$E_h^j = \sum_x \sum_y [f_{LH}^{(j)}(x,y)]^2 , \quad j = 1, 2, \ldots, J \tag{1b}$$

The energy of the vertical detail subimage at level $j$:

$$E_v^j = \sum_x \sum_y [f_{HL}^{(j)}(x,y)]^2 , \quad j = 1, 2, \ldots, J \tag{1c}$$

The energy of the diagonal detail subimage at level $j$:

$$E_d^j = \sum_x \sum_y [f_{HH}^{(j)}(x,y)]^2 , \quad j = 1, 2, \ldots, J \tag{1d}$$

The total energy of the image $f(x,y)$ in $J$ multiresolution levels is given by

$$E = E_s^J + \sum_{j=1}^{J} E_h^j + \sum_{j=1}^{J} E_v^j + \sum_{j=1}^{J} E_d^j \tag{2}$$

The normalized energy of each decomposed subimage is defined as:

$$E_S = \frac{E_s^J}{E} \tag{3a}$$

$$E_H = \frac{1}{E} \sum_{j=1}^{J} E_h^j \tag{3b}$$

$$E_V = \frac{1}{E} \sum_{j=1}^{J} E_v^j \tag{3c}$$

$$E_D = \frac{1}{E} \sum_{j=1}^{J} E_d^j \tag{3d}$$

$$E_S + E_H + E_V + E_D = 1$$

where $E_S$ is the normalized energy of the smooth subimage, and $E_H$, $E_V$ and $E_D$ are the normalized energies of the horizontal, vertical and diagonal detail subimages, respectively. As aforementioned, the normalized energy $E_S$ of an isotropic pattern is significantly larger than that of an oriented pattern. Let $\hat{f}(x,y)$ represent a restored image. We can easily set up a threshold $T_S$ to determine whether the smooth subimage should be adopted for reconstruction. This results in the following subimage selection rule.

**Subimage selection rule I:**

$$\hat{f}(x,y) = W^{-1}[f_{LL}^{(J)}] \quad if \quad E_S > T_S$$

For a texture with $E_S < T_S$, it is classified as an oriented pattern. The detail subimages with high normalized-energy values ($E_H$, $E_V$ and/or $E_D$) contain the directional information of the original image, and they should be eliminated in the reconstruction process so that the repetitive pattern will not be present in the restored image. Therefore, only the detail subimages with low normalized energy values should be included for reconstruction. For an oriented pattern containing all horizontal, vertical and diagonal directions, the three normalized energies $E_H$, $E_V$ and $E_D$ will have approximately equal magnitudes. Reconstruction from any combination of the three detail subimages cannot remove the repetitive line pattern in the image. In this case, the smooth subimage instead of the detail subimages is selected for reconstruction. This results in the second subimage selection rule below.

**Subimage selection rule II:**

**Let** $D_{\max} = \max\{E_H,\ E_D,\ E_V\}$

$$\hat{f}_H(x,y) = \begin{cases} W^{-1}[f_{LH}^{(1)}] & if\ \dfrac{E_H}{D_{\max}} < T_D \\ 0 & otherwise \end{cases}$$

$$\hat{f}_V(x,y) = \begin{cases} W^{-1}[f_{HL}^{(1)}] & if\ \dfrac{E_V}{D_{\max}} < T_D \\ 0 & otherwise \end{cases}$$

$$\hat{f}_D(x,y) = \begin{cases} W^{-1}[f_{HL}^{(1)}] & if\ \dfrac{E_D}{D_{\max}} < T_D \\ 0 & otherwise \end{cases}$$

$$\hat{f}(x,y) = \hat{f}_H(x,y) + \hat{f}_V(x,y) + \hat{f}_D(x,y)$$

$$\hat{f}\ (x,y)=\begin{cases}\hat{f}(x,y) & \textit{if } \hat{f}(x,y)\neq 0 \textit{ for some } (x,y)\\ W^{-1}[f_{LL}^{(J)}] & \textit{otherwise}\end{cases}$$

In subimage selection rule II, the threshold $T_D$ is used to detect the significance of directionality in detail subimages. If the ratio of a normalized energy to $D_{\max}$ is less than the threshold $T_D$, the corresponding detail subimage contains no such directional line in the original image. It is therefore used for reconstruction. If all three detail subimages have their energy ratios larger than the threshold $T_D$, then the original image must contain all three horizontal, vertical and diagonal directions, and only the smooth subimage is finally selected for reconstruction. Subimage selection rule II is carried out only if subimage selection rule I fails. Note that the choice of the threshold $T_S$ in subimage selection rule I is not at all crucial, because the mechanism of selection rule II allows an isotropic texture to use the smooth subimage for reconstruction. The choice of threshold $T_D$ is also not crucial because the detail subimage that contains no directional information of the original image has distinctly small energy value. In this study, the threshold values of $T_S$ used in selection rule I, and $T_D$ used in selection rule II are empirically set at 0.96 and 0.35, respectively, at the third multiresolution level ($J$ = 3). Figure 4 illustrates the detailed flow diagram of the subimage selection procedure for image reconstruction.

Figure 5(a) shows a structural texture with repetitive vertical line pattern. Figure 5(b) presents the decomposition result of one multiresolution level, where $f_{LL}(x',y')$, $f_{LH}(x',y')$, $f_{HL}(x',y')$, and $f_{HH}(x',y')$ are shown in the lower-left, upper-left, lower-right and upper-right quadrants, respectively. It can be seen from Figure 5(b) that the vertical detail subimage preserves the vertical edges and has relatively large energy value. Table 1(a) lists the normalized energy of each decomposed subimage in three multiresolution levels. Note that the normalized energies $E_D$ (diagonal subimage) and $E_H$ (horizontal subimage) are approximately zero, and $E_V$ (vertical subimage) is distinctly large with respect to $E_D$ and $E_H$. Figure 5(c) shows that the reconstruction from the selected horizontal and diagonal subimages sufficiently eliminates all repetitive vertical lines.

Figure 6(a) shows a statistical texture of sandpaper with coarse grains. Figure 6(b) presents its four decomposed subimages at multiresolution level 1, and shows that all three high frequency subbands result in uniform images with low gray levels (i.e., low wavelet coefficients). Table 1(b) lists the normalized energy values of all decomposed subimages in three resolution levels. As we can see from Table 1(b), $E_H$, $E_V$ and $E_D$ of the horizontal, vertical and diagonal subimages are approximately equally distributed. Since the normalized energy $E_S$ of the smooth subimage is sufficiently large, the smooth subimage is selected for reconstruction. Figure 6(c) shows the reconstruction result from the smooth subimage at resolution level 3 (i.e.,$W^{-1}[f_{LL}^{(3)}]$). Figure 7(a) shows a textile fabric. The weave pattern of the textile fabric can be visually classified as a structural texture with two directions (warp and woof directions). By analyzing the fabric image in the Fourier domain, as seen in Figure 7(b), we found that the textile fabric presents four directions: horizontal, vertical, $45^{o}$-diagonal and $135^{o}$-diagonal. Table 1(c) reveals that the energy values $E_H$, $E_V$ and $E_D$ of the three detail subimages are similar to one another, and the $E_S$ value of the smooth subimage is as high as 0.98 at resolution level 3. Therefore, the smooth subimage, instead of the combination of detail subimages, of the textile fabric is adopted for reconstruction. Figure 7(d) demonstrates the reconstruction result of the textile fabric from the smooth subimage at resolution level 3.

## 2.3 Automatic Selection of Multiresolution Levels

As aforementioned, decomposition of a textured image in its proper resolution will effectively eliminate repetitive patterns and highlight the local anomalies. For structural textures with high directionality, the oriented patterns in horizontal, vertical and diagonal directions are well separated in the first decomposition level (i.e., $J = 1$). The repetitively oriented pattern can be immediately removed from the reconstruction of detail subimages at resolution level 1. The larger decomposition levels of an image only generate coarser representation of the oriented pattern in each of the three detail subimages. Therefore, the reconstruction process for selective detail subimages is only required at resolution level 1.

For statistical textures with isotropic patterns or structural textures containing all horizontal, vertical and diagonal orientations, the smooth subimage is used for reconstruction. Therefore, the choice of a proper multiresolution level is crucial for the success of background-texture removal. The larger the number of resolution levels is used, the better uniformity of gray levels will be obtained in the restored image. However, too large the number of multiresolution levels will generate the fusion effect for the anomalies, and may cause localization error of the detected defect.

The choice of a proper number of multiresolution levels is based on the energy ratio of detail subimages in two consecutive levels. Let $D_j$ be the normalized energy sum of the three detail subimages at resolution level *j*, i.e.,

$$D_j = (E_h^j + E_v^j + E_d^j) / E \tag{4}$$

and $R_j$ the energy ratio of detail subimages between resolution levels *j* and *j*-1, i.e.,

$$R_j = \frac{D_j}{D_{j-1}} \quad , \quad j = 1, 2, \ldots, J_{\max} \tag{5}$$

where $J_{\max}$ is the maximum decomposition level. In practice, the value of $J_{\max}$ is generally no more than 6. The best number of multiresolution level $J^*$ is chosen such that $R_{J^*}$ is a minimum, i.e.,

$$J^* = arg\{\min_j\{R_j\}\}$$

The minimum value of $R_j$ represents that the high frequency components between two consecutive decomposition levels are sufficiently separated in terms of marginal improvement, and the decomposition process should be stopped. For multiresolution level $j < J^*$, $R_j$ indicates that some detail (high frequency) components still remain in the coarse approximation, and the smooth subimage should be further decomposed. For multiresolution level $j > J^*$, $R_j$ indicates that the high frequency components are over smoothed from its coarse approximation, and the reconstruction result from such smooth subimage will cause fusion effects for defective textures.

Figure 8(a) shows the original image of a sandpaper texture, and Figures 8(b)-(f) demonstrate the restoration results from the smooth subimage, i.e., $W^{-1}[f_{LL}^{(J)}]$, at resolution levels *J* = 1, 2, 3, 4 and 5, respectively. Table 2 lists the statistics of $E_S$ (normalized energy of the smooth subimage), $D_j$ (normalized energy sum of three detail subimages) and $R_j$ (energy ratio) at various levels. It shows that $R_j$ reaches its minimum at resolution level $J$ = 4 ($R_4$ = 1.284). For multiresolution levels $J$ = 1 and 2, the restored images, as shown in Figures 8(b) and 8(c), still resemble to their original image (Figure 8(a)), and the regular texture pattern is not removed. The restored image at level 3 (Figure 8(d)) starts to smooth the sandpaper texture, and the restored image at level 4 (Figure 8(e)) sufficiently removes the regular texture pattern. Although the restored image at level 5 (Figure 8(f)) generates the most uniform surface pattern, it may result in fusion effects for defective textures in the inspection process.

## 3. EXPERIMENTAL RESULTS

In this section, we present the experimental results from a variety of structural and statistical textures to evaluate the efficacy of the proposed method. The proposed algorithms are implemented on a personal computer. The images are 256 × 256 pixels wide with 8-bit gray levels. Throughout the experiments, all test samples used the 8-tap Symmlets (S8) as the wavelet bases, and used the thresholds $T_S$ = 0.96 for subimage selection rule I, and $T_D$ = 0.35 for subimage selection rule II. The normalized energies (eqs. (3a)-(3d)) are computed at resolution level 3 ($J$ = 3).

In a restored image, the intensity variation in homogeneous regions will be very small, whereas the intensity variance of defective regions is distinctly large with respect to the entire restored image. To visualize and localize texture defects in the restored image, we use the simple statistical process control limits for distinguishing anomalies from the uniform pattern in the restored image. The upper and lower control limits for intensity variation in the restored image are given by

$$\mu_{\hat{f}} \pm k\delta_{\hat{f}}$$

where $\mu_{\hat{f}}$ and $\delta_{\hat{f}}$ are the mean and standard deviation of gray levels in the restored image $\hat{f}(x,y)$, and $k$ is a control constant. In this paper, we have used $k$ = 3 to follow the typical 3-sigma standard in the statistical process control. Pixels in homogeneous regions (within the control limits) and pixels in defective regions (outside the control limit) are, respectively, represented by black and white intensities so that defects can be observed in the binarized image.

For structural textures with high directionality, Figure 9(a) shows a defect-free machined surface with vertical feedmarks. It can be seen from Table 3(a) that the energy $E_S$ of the smooth subimage at resolution level 3 is lower than the threshold $T_S$, and the energy $E_V$ of the vertical detail subimage is distinctly larger than $E_H$ of the horizontal detail subimage and $E_D$ of the diagonal detail subimage. Therefore, the horizontal and diagonal detail subimages at resolution level 1 are chosen for reconstruction, i.e., $W^{-1}[f_{LH}^{(1)}]+W^{-1}[f_{HH}^{(1)}]$. Figure 9(b) presents the reconstruction result of the defect-free machined surface. Note that the vertical feedmarks are sufficiently removed in the restored image. Figure 9(c) shows a defective version of the machined surface. Figures 9(d) and 9(e) demonstrate the reconstruction and binarization results, respectively, based on the selected detail subimages. It shows that the scratch defect is well detected in the binarized image.

Figure 10(a) presents a defect-free wood surface with less regular horizontal stripes. Table 3(b) shows that the energy $E_S$ at resolution level 3 is smaller than the threshold $T_S$, and the energy $E_H$ is significantly larger than $E_V$ and $E_D$.

Therefore, vertical and diagonal detail subimages at resolution level 1 are selected for reconstruction, i.e., $W^{-1}[f_{HL}^{(1)}]+W^{-1}[f_{HH}^{(1)}]$. Although the horizontal line pattern of the wood surface is not as regular as that of the machined surface, the restored image shown in Figure 10(b) has sufficiently eliminated the horizontal stripes. Figure 10(c) presents the wood surface with a wear defect. The reconstruction and binarization results, as seen in Figures 10(d) and 10(e), have reliably shown the wear defect on the wood surface.

For structural textures with multiple directions, Figure 11(a) presents a defect-free wool fabric. Table 4 shows that the energy $E_S$ of the smooth subimage at resolution level 3 is as high as 0.98, and the minimum energy ratio $R_j$ is obtained at resolution level 4 for the fabric sample. Therefore, the smooth subimage at resolution level 4, i.e., $W^{-1}[f_{LL}^{(4)}]$, is selected for reconstruction. Figure 12(a) illustrates the defective version of the fabric. As seen in Figures 12(b)-(c), the reconstruction result from the smooth subimage at resolution level 4 reveals that the shedding defects in the fabric is reliably detected.

For statistical textures, Figure 13(a) shows a defect-free surface of sandpaper with fine grains. As seen in Table 5(a), we found that the energy $E_S$ of the smooth image at resolution level 3 is only 0.89, which is lower than the threshold $T_S$. Owing to the extra-fine textured surface of the sandpaper, the high frequency subbands also possess significant energy magnitude. Since the energy values $E_H$, $E_V$ and $E_D$ of the three detail subimages are similar to one another, the smooth subimage, instead of the detail subimages, is eventually chosen for reconstruction. Table 5(b) shows that the energy ratio $R_j$ reaches its minimum at resolution level 3.

Figure 13(b) presents the reconstruction result of the defect-free sandpaper using $W^{-1}[f_{LL}^{(3)}]$. Figures 13(c) and 13(d) show two defective versions of the fine sandpaper, one with a linear defect (scratch) and the other one with a random defect (wear). The reconstruction and binarization results of these two defective sandpaper surfaces are shown in Figures 13(e)-(h). The defects in the surfaces are well detected and located from the reconstruction of the smooth subimage at resolution level 3.

In our empirical study, the proposed method has been used to test 8 different structural textures that involve 22 images of varied defects, and 6 different statistical textures that involve 19 images of varied defects. The detection results of the 41 test images from the proposed method are similar to those from manual segmentation.

Figures 14 and 15 further demonstrate two structural textures of bamboo weave and wool weave. Figures 16 and 17 present two statistical textures of cast surface and wool material. The additional texture samples in Figures 15-17 are less regular in terms of degrees of periodicity and self-similarity. The detection results show that a highly regular texture such as the bamboo weave pattern in Figure 14 will yield high uniform image in the reconstruction. Less regular textures such as the cast and wool surfaces in Figures 15-17 have residuals of background textures in the restored images. However, the resulting binary images, as shown in Figures 15(c), 16(c) and 17(c), can still effectively identify the defects, although some noisy spots appear in the binarized images. The experimental results have shown that the proposed method is well suited for homogeneous textures that contain regular patterns. Its performance will be degraded for irregular textures. It may fail to detect subtle anomalies in highly irregular textures such as granite surfaces.

In order to show the effect of changes in illumination, Figures 18(a1) and (a2) show, respectively, the underexposed and overexposed versions of the structural texture of bamboo weave in Figure 14(a). In addition, Figures 19(a1) and (a2) present the underexposed and overexposed versions of the statistical texture of sandpaper in Figure 13(d). The corresponding detection results, as shown in Figures 18 and 19, reveal that the proposed automatic wavelet band selection scheme for image reconstruction is insensitive to changes in illumination. The defects are reliably detected for textures under varied illuminations. Based on the experimental results from both structural and statistical textures, the proposed method for automatic selection of decomposed subimages and the number of multiresolution levels has shown its efficacy to set up the reconstruction process for the detection of local defects in homogeneous textures.

## 4. CONCLUSIONS

In this paper, we have successfully proposed an automatic band selection procedure that determines the best decomposed subimages and the number of multiresolution levels for image reconstruction in the wavelet transform domain. Local defects embedded in a homogeneous texture can be effectively detected by removing the global repetitive texture pattern in the image.

The energies of the wavelet coefficients distributed in different frequency channels at various decomposition levels provide unique information about texture characteristics. Textures with high-energy response in the smooth subimage ($E_S$), or with approximately equal energy values in three detail subimages ($E_H$, $E_V$ and $E_D$), the smooth subimage is chosen for reconstruction. The energy ratio $R_j$ between two consecutive decomposition levels is further used to automatically determine the best decomposition level so that the restored image can effectively remove repetitive patterns without causing fusion effects in defective textures. Oriented textures containing single or two directions possess relatively high-energy values in their corresponding detail subimages. The energy value of the smooth subimage is relatively low, and the dominant detail subimage(s) is (are) excluded in the reconstruction process. Oriented textures with significant dominant high-frequency channels have their directional patterns well separated in the first decomposition level. The non-dominant detail subimage(s) at resolution level 1 is (are) therefore used for reconstruction.

The proposed automatic wavelet band selection procedure for image reconstruction works successfully for structural and statistical textures with homogeneous patterns. The decomposed subimages and the number of multiresolution levels determined by the automatic band selection scheme are similar to the manual selection results. The proposed method accomplished in this study can alleviate human intervention for defect inspection in homogeneously textured images.

## REFERENCES

1. L. H. Siew and R. M. Hogdson, Texture measures for carpet wear assessment, *IEEE Trans. Pattern Anal. Mach. Intell.* 10 (1988) 92-105.

2. R. W. Conners, C. W. McMillin, K. Lin and R. E. Vasquez-Espinosa, Identifying and locating surface defects in wood, *IEEE Trans. Pattern Anal. Mach. Intell.* PAMI-5 (1983) 573-583.

3. K. V. Ramana and B. Ramamoorthy, Statistical methods to compare the texture features of machined surfaces, *Pattern Recognition* 29 (1996) 1447-1459.

4. S. -S. Liu and M. E. Jernigan, Texture analysis and discrimination in additive noise, *Computer Vision, Graphics, Image Process.* 49 (1990) 52-67.

5. R. Azencott, J. -P. Wang and L. Younes, Texture classification using windowed Fourier filters, *IEEE Trans. Pattern Anal. Mach. Intell.* 19 (1997) 148-153.

6. H. Arof and F. Deravi, Circular neighborhood and 1-D DFT features for texture classification and segmentation, *IEE Proceedings: Vision, Image and Signal Processing* 145 (1998) 167-172.

7. M. Zou and D. Wang, Texture identification and image segmentation via Fourier transform, *Proceedings of SPIE*, V. 4550, Wuhan, China, 2001, pp. 34-39.

8. J. G. Daugman, Uncertainty relation for resolution in space, spatial-frequency, and orientation optimized by two dimensional visual cortical filters, *J. Opt. Soc. Am.* 2 (1985) 1160-1169.

9. M. Clark and A. C. Bovik, Texture segmentation using Gabor modulation/ demodulation, *Pattern Recognition Letters* 6 (1987) 261-267.

10. D. Dunn, W. Higgins and J. Wakeley, Texture segmentation using 2-D Gabor elementary function, *IEEE Trans. Pattern Anal. Mach. Intell.* 16 (1994) 130-149.

11. A. Teuner, O. Pichler and B. J. Hosticka, Unsupervised texture segmentation of images using tuned matched Gabor filters, *IEEE Trans. Image Processing* 4 (1995) 863-870.

12. P. P. Raghu and B. Yegnanarayana, Segmentation of Gabor-filtered textures using deterministic relaxation, *IEEE Trans. Image Processing* 5 (1996) 1625-1636.

13. J. Escofet, R. B. Navarro, M. S. Millan and J. M. Pladellorens, Detection of local defects in textile webs using Gabor filter, *Proceedings of SPIE*, V. 2785, Bellingham, WA, 1996, pp. 163-170.

14. A. Kumar and G. K. H. Pang, Defect detection in textured materials using Gabor filters, *IEEE Trans. Industry Applications* 38 (2002) 425-440.

15. D. Dunn and W. E. Higgins, Optimal Gabor filters for texture segmentation, *IEEE Trans. Image Processing* 4 (1995) 947-964.

16. T. P. Weldon, W. E. Higgins and D. F. Dunn, Efficient Gabor filter design for texture segmentation, *Pattern Recognition* 29 (1996) 2005-2015.

17. P. G. Lemarie and Y. Meyer, Ondelettes et bases Hilbertiennes, *Rev. Mat. Ibero Americana* 2 (1986) 1-18.

18. S. G. Mallat, A theory for multiresolution signal decomposition: the wavelet representation, *IEEE Trans. Pattern Anal. Mach.* Intell. 11 (1989) 674-693.

19. A. Laine and J. Fan, Texture classification by wavelet packet signatures, *IEEE Trans. Pattern Anal. Mach. Intell.* 15 (1993) 1186-1191.

20. M. Unser, Texture classification and segmentation using wavelet frames, *IEEE Trans. Image Processing* 4 (1995) 1549-1560.

21. Y. Chitre and A. P. Dhawan, M-band wavelet discrimination of natural textures, *Pattern Recognition* 32 (1999) 773-789.

22. G. Lambert and F. Bock, Wavelet methods for texture defect detection, *IEEE International Conference on Image Processing*, V. 3, Santa Barbara, CA, 1997, pp. 201-204.

23. A. L. Amet, A. Ertuzun and A. Ercil, Texture defect detection using subband domain co-occurrence matrices, *Image Analysis and Interpretation* 1 (1998) 205-210.

24. K. Y. Song, M. Petrou and J. Kittler, Texture defect detection: a review, *Proceedings of SPIE*, V. 1708, Orlando, FL, 1992, pp. 99-106.

25. K. Y. Song, J. Kittler, M. Petrou and I. Ng., Chromato-structural approach toward surface defect detection in random textured images, *Proceedings of SPIE*, V. 2183, San Jose, CA, 1994, pp. 193-204.

26. K. Y. Song, J. Kittler and M. Petrou, Defect detection in random colour textures, *Image and Vision Computing* 14 (1996) 667-683.

27. I. Ng, J. Kittler and J. Illingworth, Supervised segmentation using a multiresolution data representation, *Signal Processing* 31 (1993) 133-163.

28. F. S. Cohen, Maximum likelihood unsupervised textured image segmentation, *GVGIP* : *Graphical Models and Image Processing* 54 (1992) 239-251.

29. M. M. Van Hulle and T. Tollenaere, A modular artificial neural network for texture processing, *Neural Networks* 6 (1993) 7-32.

30. I. Daubechies, *Ten Lectures on Wavelets*, SIAM, Philadelphia, PA, 1992.

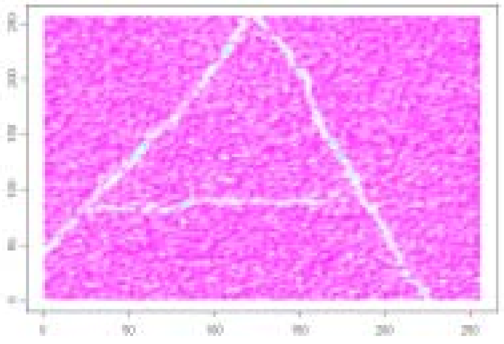

(a) Original image

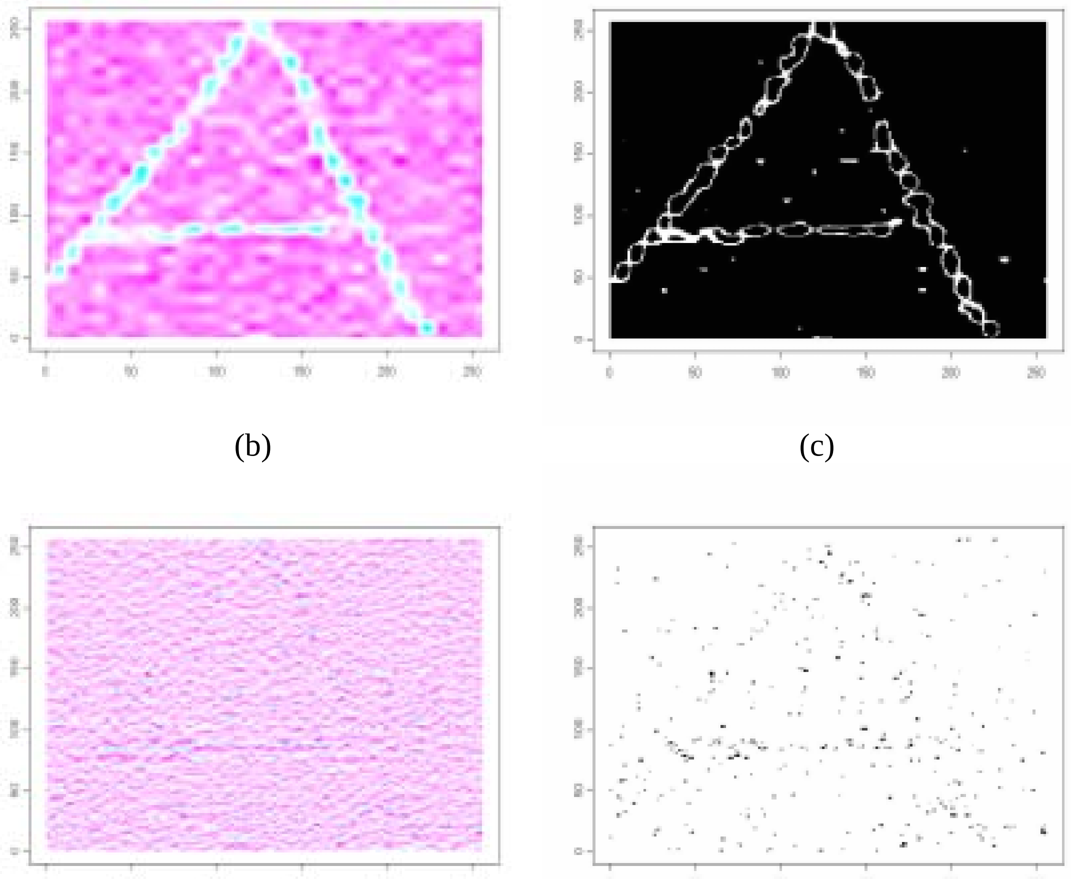

(b) (c)

(d) (e)

Figure 1. The effect of selective subimages on image reconstruction for the sandpaper with scratch defects: (a) the original image; (b) the restored image from the smooth subimage; (c) the binarized image of (b); (d) the restored image from the three detail subimages; (e) the binarized image of (d).

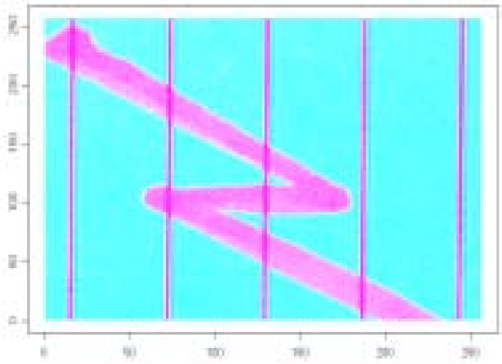

(a) Original image

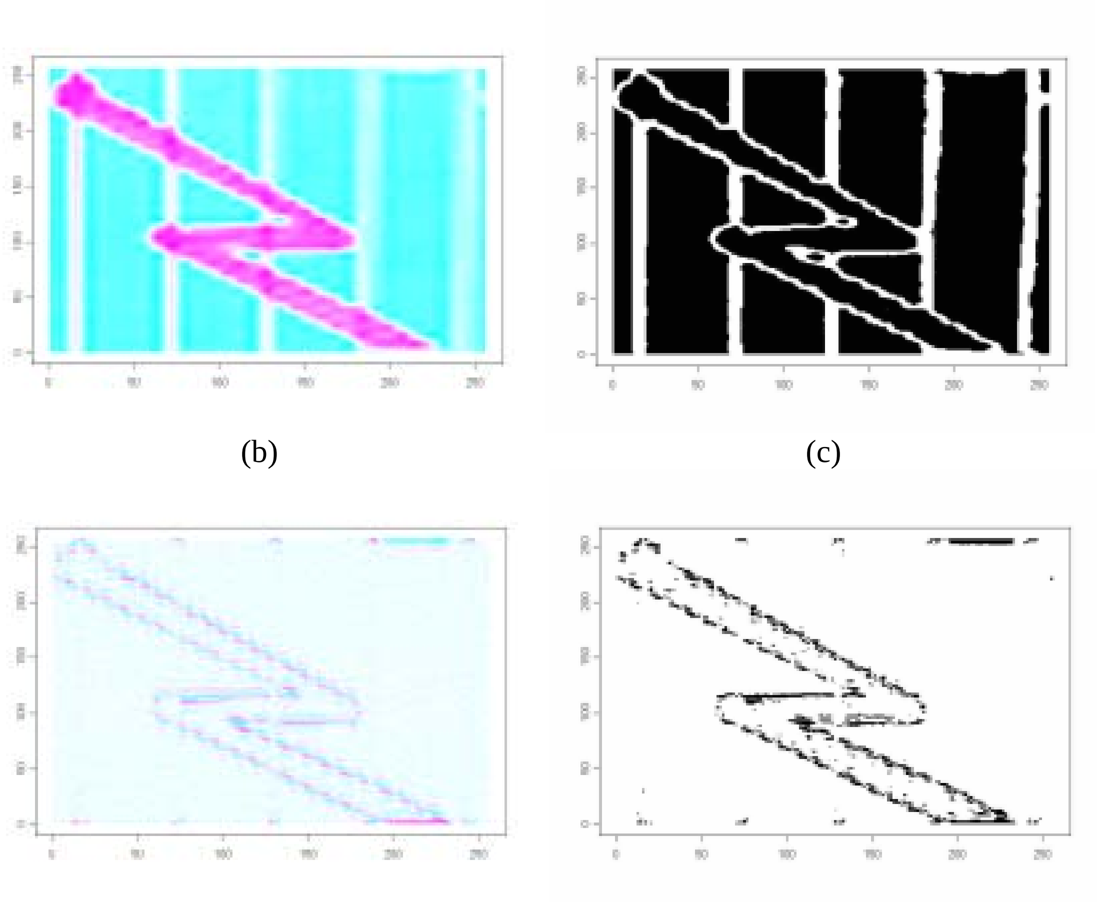

(b) (c)

(d) (e)

Figure 2. The effect of selective subimages on image reconstruction for the line-structured texture with a line defect: (a) the original image; (b) the restored image from the smooth subimage; (c) the binarized image of (b); (d) the restored image from the horizontal and diagonal detail subimages; (e) the binarized image of (d).

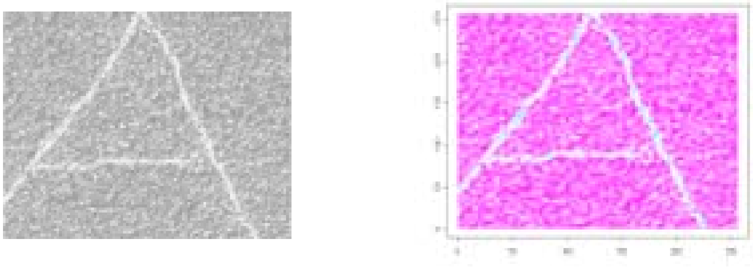

(a) Original image

(b) J=2

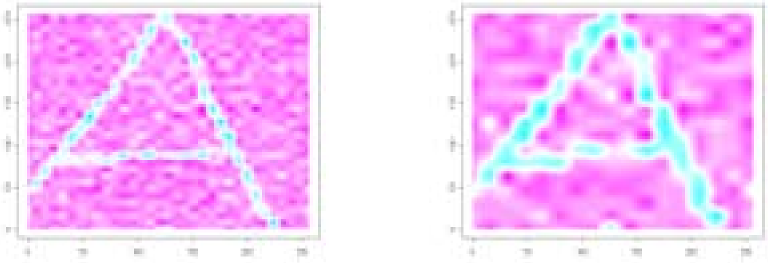

(c) J=3

(d) J=4

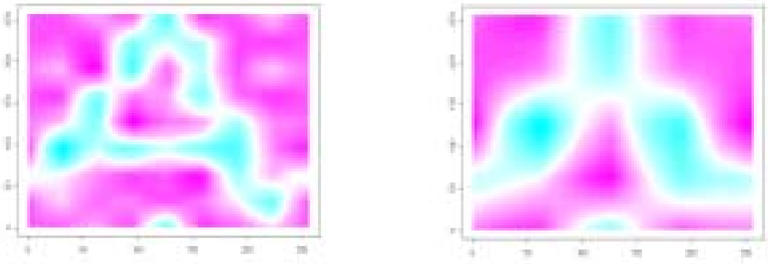

(e) J=5

(f) J=6

Figure 3. The effect of varying number of multiresolution levels on image reconstruction: (a) the original sandpaper image with scratch defects; (b) – (f) reconstruction results from multiresolution levels J = 2, 3, 4, 5 and 6, respectively. (The reconstruction is based on the smooth subimage with wavelet basis S8.)

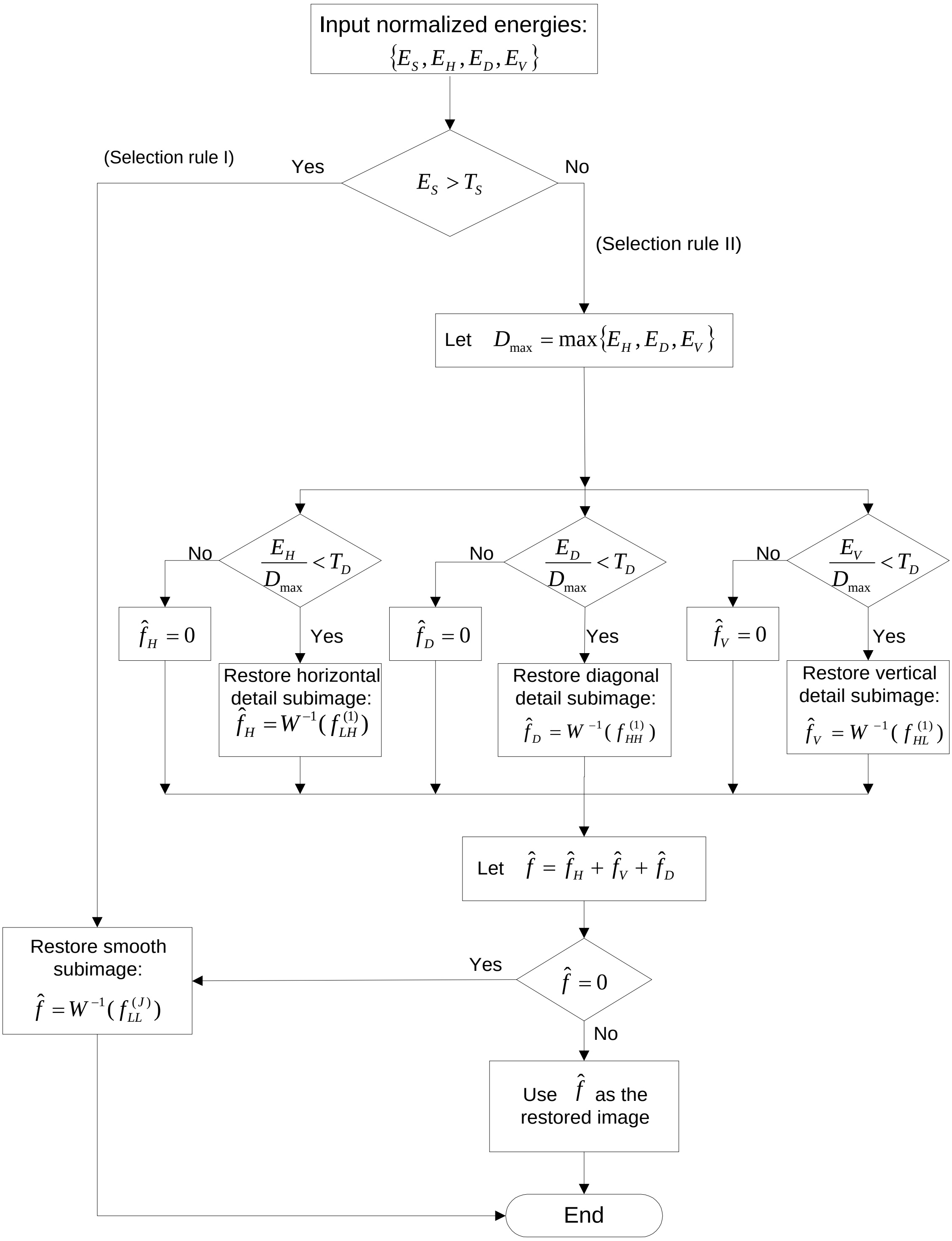

Figure 4. The procedure for the choice of decomposed subimages.

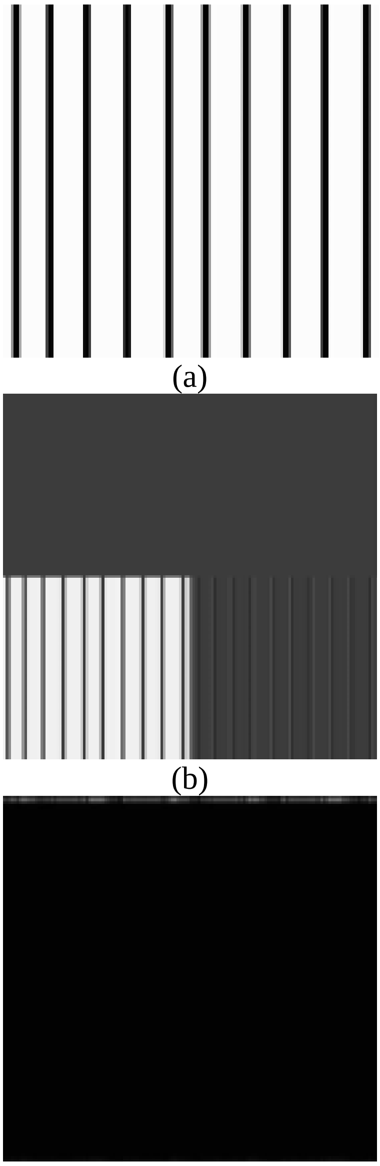

(a)

(b)

(c)

Figure 5. (a) A texture with vertical line pattern; (b) four decomposed subimages at resolution level 1; (c) the restored image from $W^{-1}(f_{LH}^{(1)}) + W^{-1}(f_{HH}^{(1)})$ .

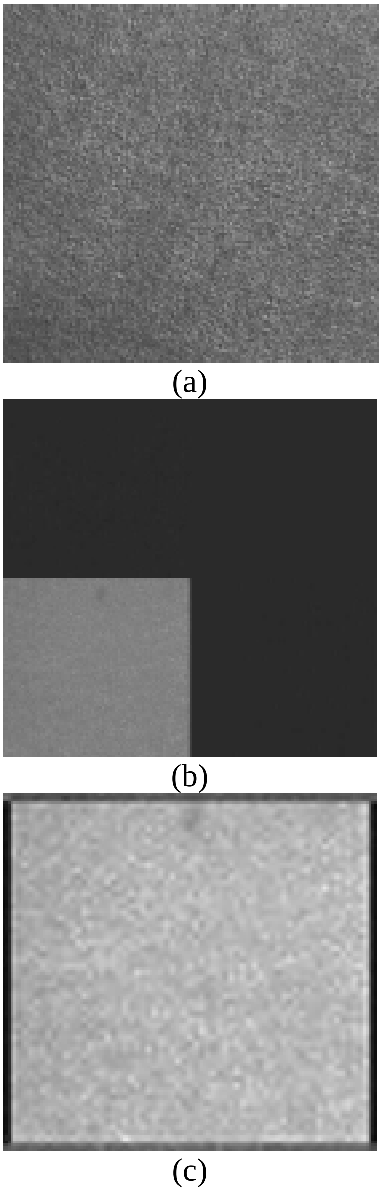

Figure 6. (a) The original sandpaper image; (b) four decomposed subimages at resolution level 1; (c) the restored image from the smooth subimage at resolution level 3.

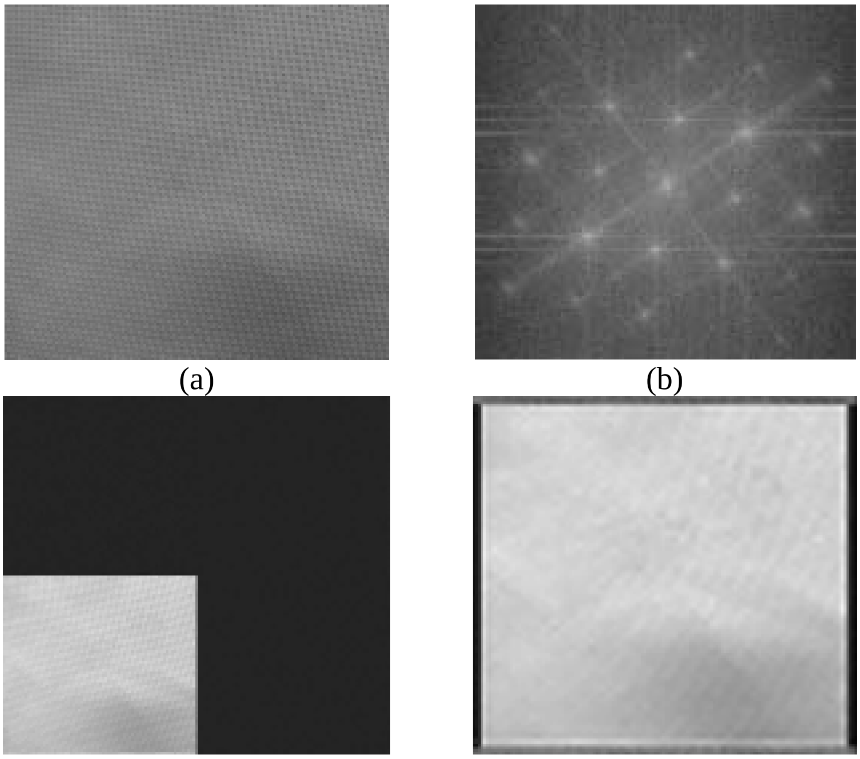

(a) (b)

(c) (d)

Figure 7. (a) The original fabric image; (b) the Fourier spectrum of (a); (c) four decomposed subumages at resolution level 1; (d) the restored image from the smooth subimage at resolution level 3.

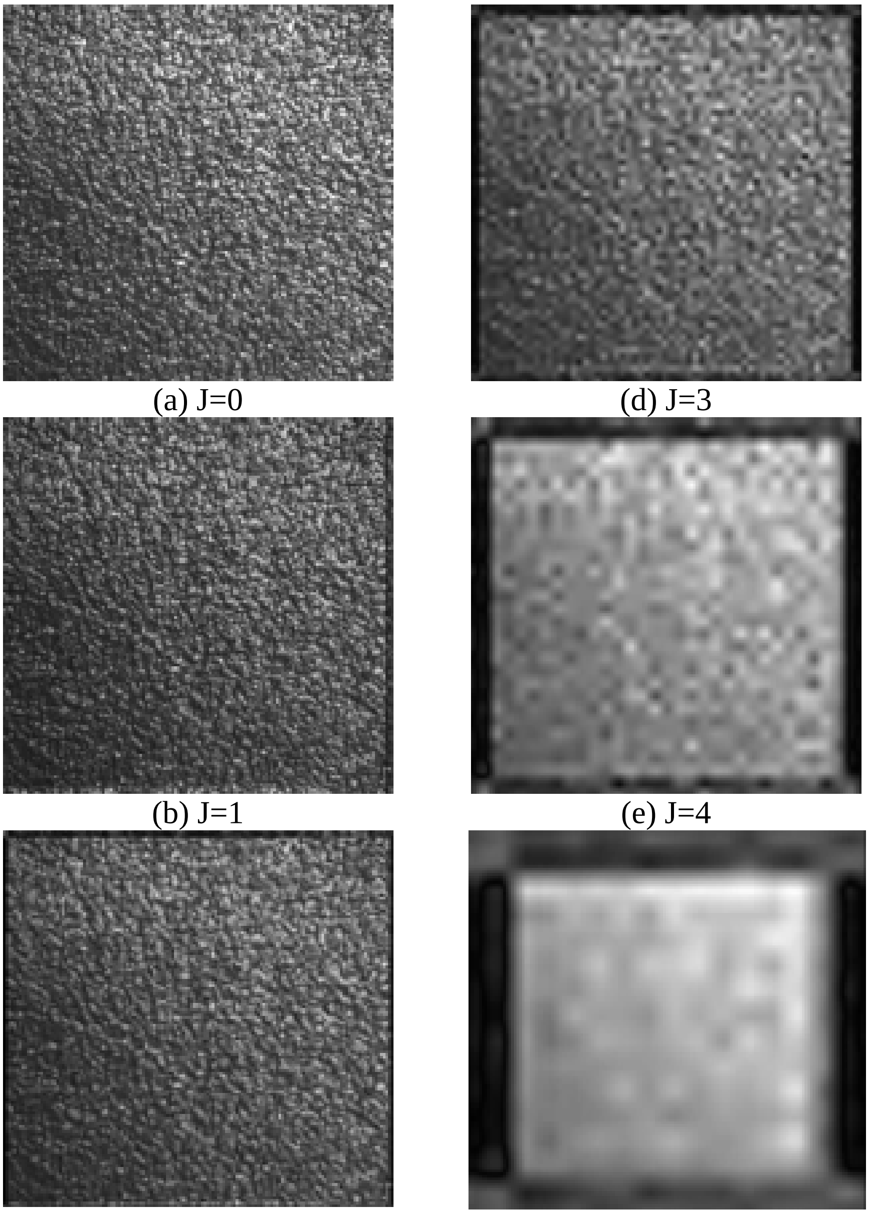

(a) J=0

(d) J=3

(b) J=1

(e) J=4

(c) J=2

(f) J=5

Figure 8. The reconstruction of a sandpaper texture from the smooth subimage at resolution level: (a) J=0 (the original image); (b) J=1; (c) J=2; (d) J=3; (e) J=4; (f) J=5.

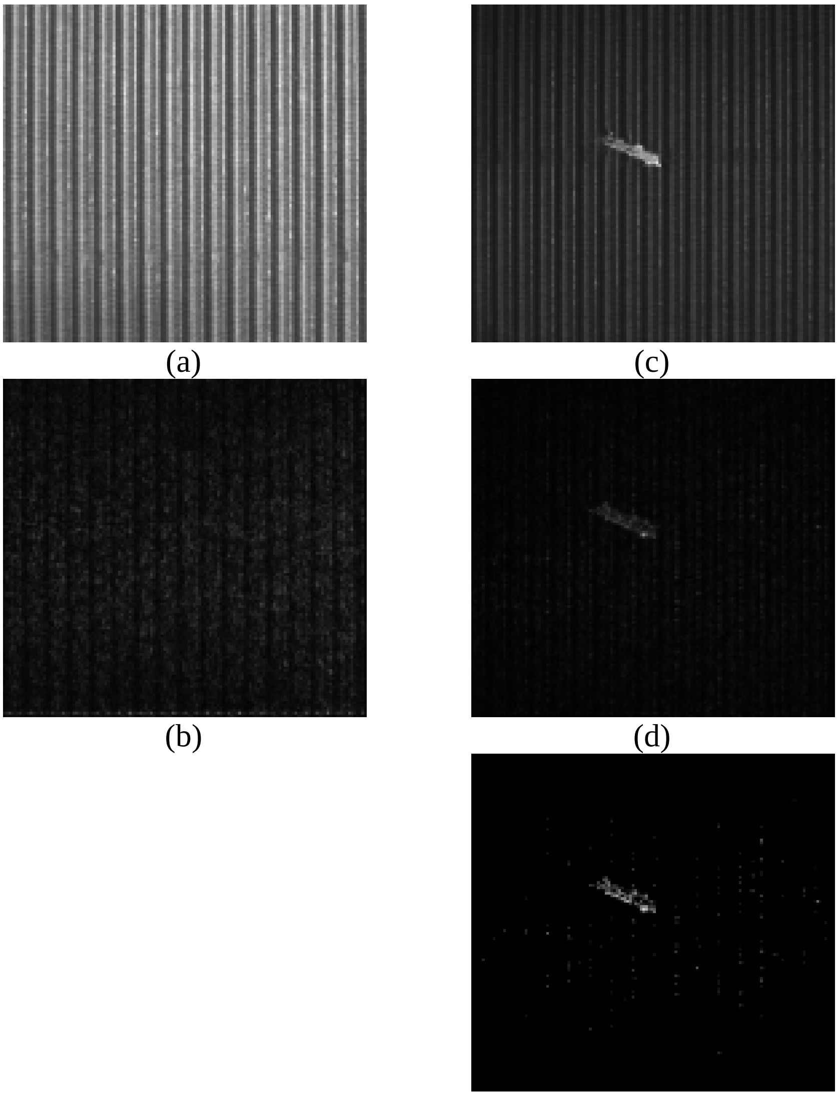

(a) (c)

(b) (d)

(e)

Figure 9. Detecting defects in a milled surface: (a) the original image of a defect-free surface; (b) the reconstruction result of (a) from the horizontal and diagonal detail subimages at resolution level 1; (c) a defective version of the milled surface; (d) the reconstruction result of (c); (e) the binarized result of (d).

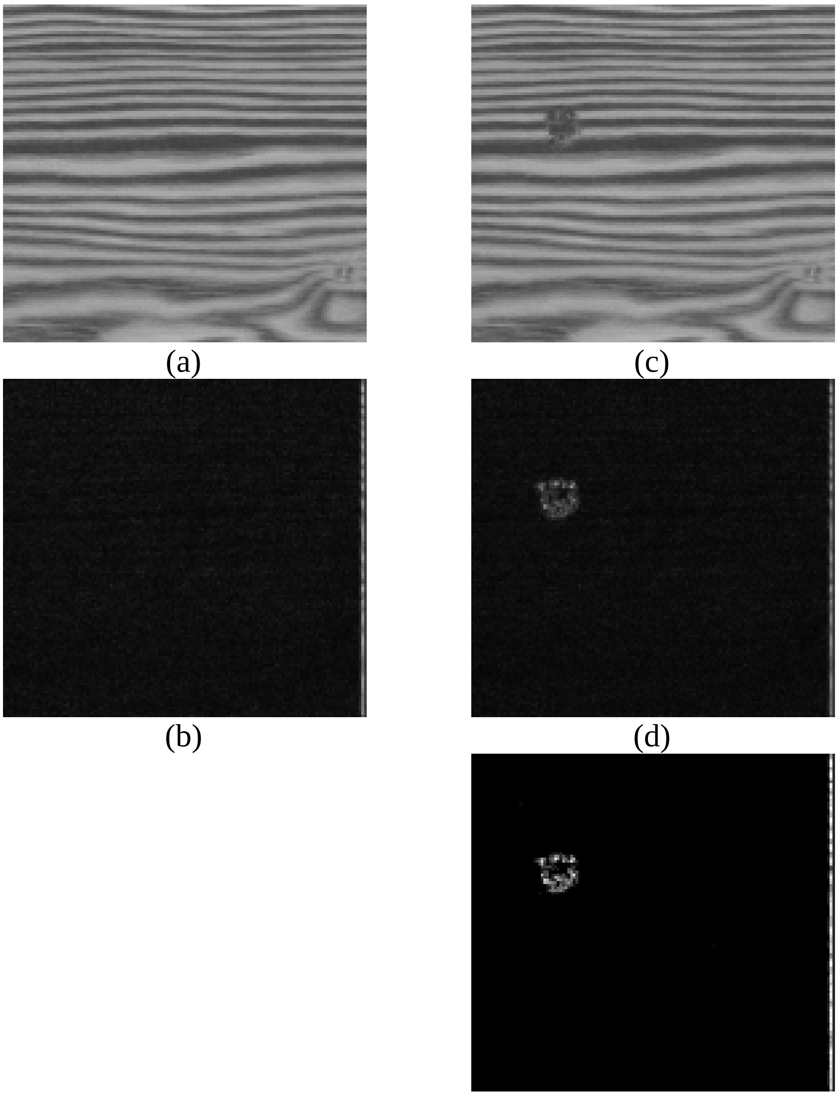
(a) (c)

(b) (d)

(e)

Figure 10. Detecting the defect in wood: (a) the original image of a defect-free surface; (b) the reconstruction result of (a) from the vertical and diagonal detail subimages at resolution level 1; (c) a defective version of the wood surface; (d) the reconstruction result of (c); (e) the binarized result of (d).

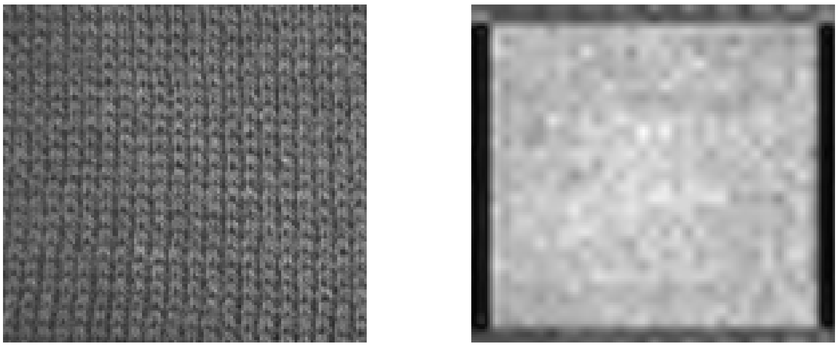

(a) (b)

Figure 11. A defect-free wool fabric: (a) the original image; (b) the reconstruction result from the smooth subimage at resolution level 4.

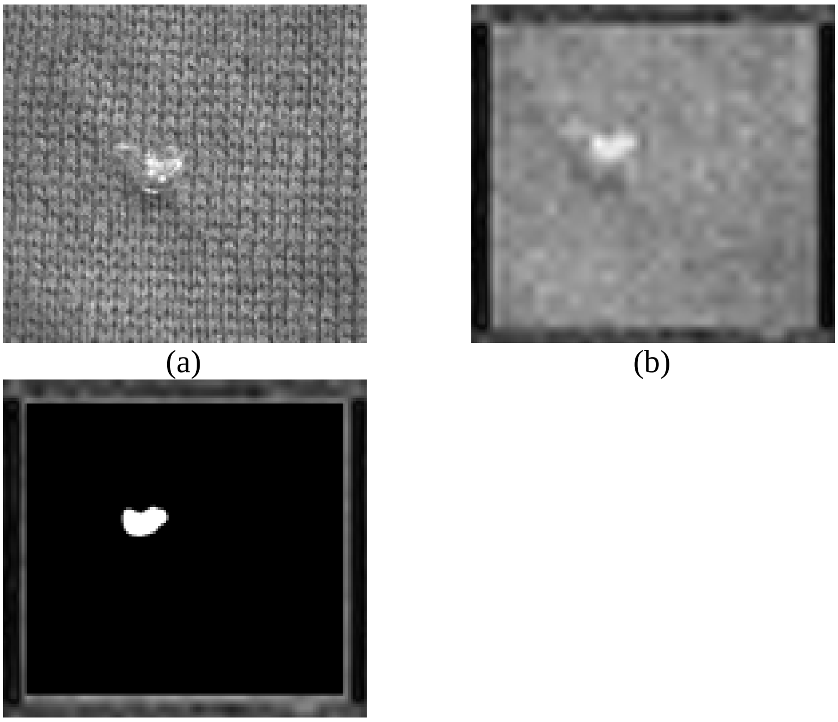

(a) (b) (c)

Figure 12. Detecting the defect in wool: (a) the defective version of the wool fabric in Figure 11(a); (b) the reconstruction result from $W^{-1}[f_{LL}^{(4)}]$; (c) the binarized result of (b).

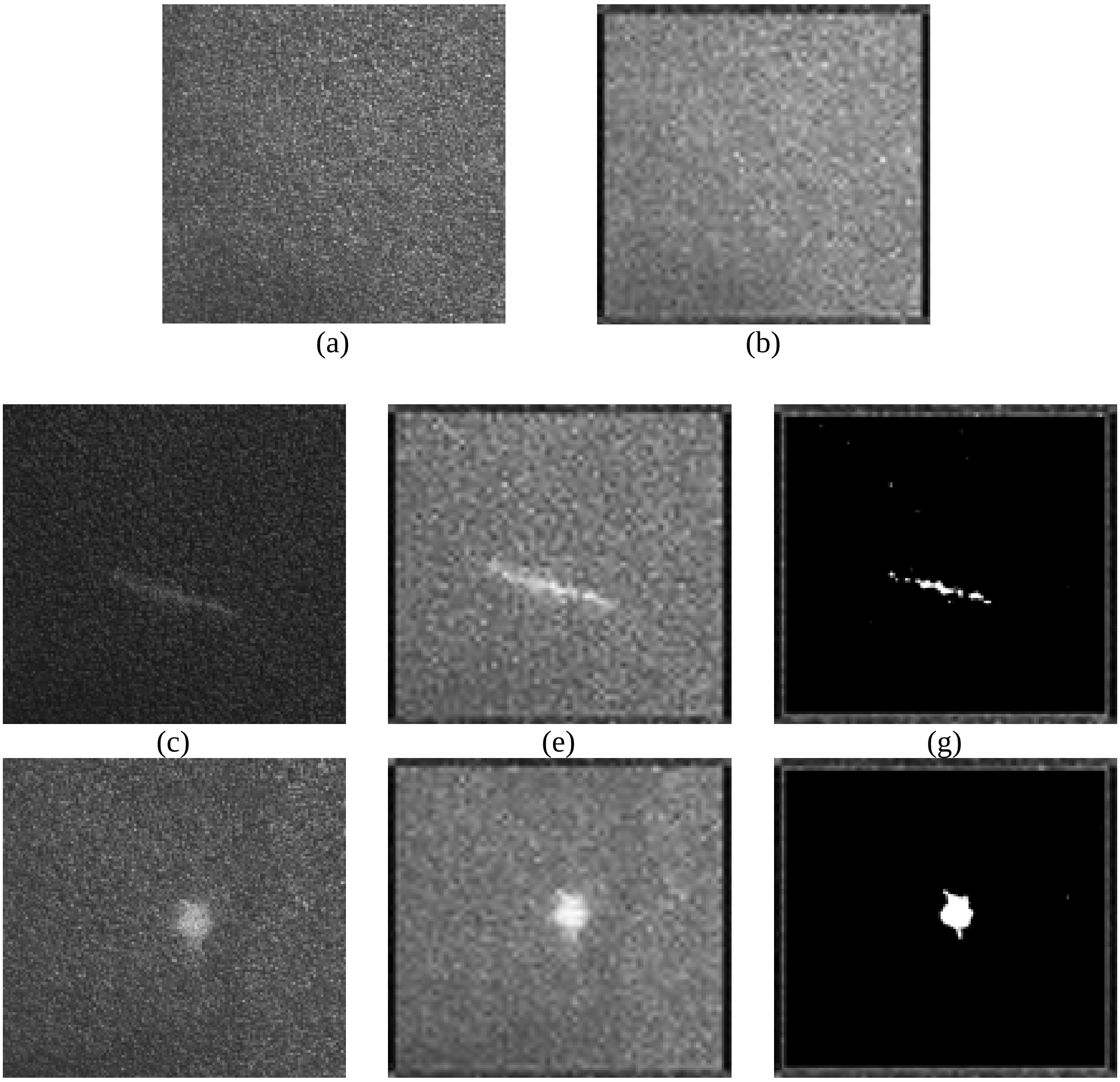
(a) (b)

(c) (e) (g)

(d) (f) (h)

Figure 13. Detecting defects in sandpaper: (a) the original sandpaper image; (b) the reconstruction result of (a) from $W^{-1}[f_{LL}^{(3)}]$; (c) the sandpaper image with a scratch defect; (d) the sandpaper image with a wear defect; (e), (f) the reconstruction results of (c) and (d); (g), (h) the binarized results of (e) and (f).

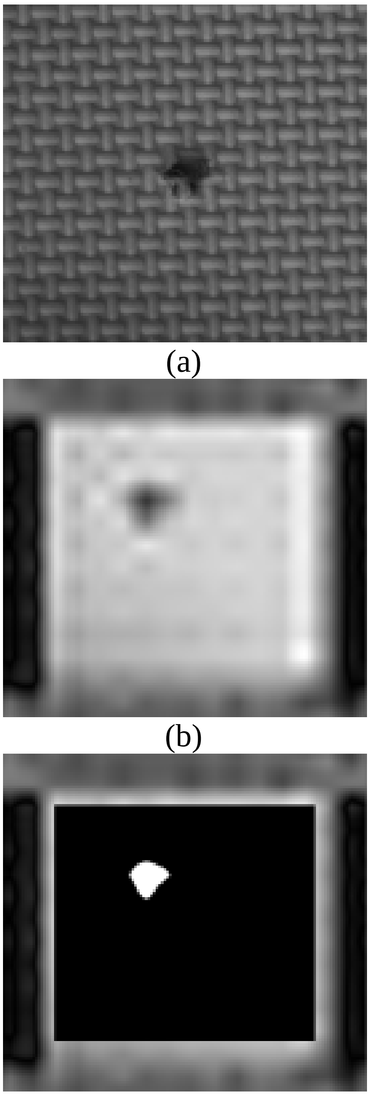

(a)

(b)

(c)

Figure 14. Detecting the defect in a bamboo weave texture: (a) a defective surface; (b) the reconstructed image; (c) the binarized result of (b).

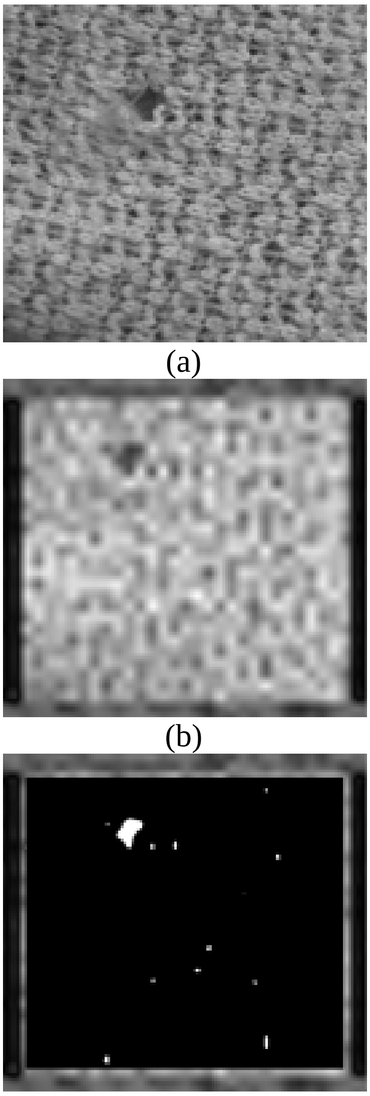

(a)

(b)

(c)

Figure 15. Detecting the defect in a wool weave texture: (a) a defective surface; (b) the reconstructed image; (c) the binarized result of (b).

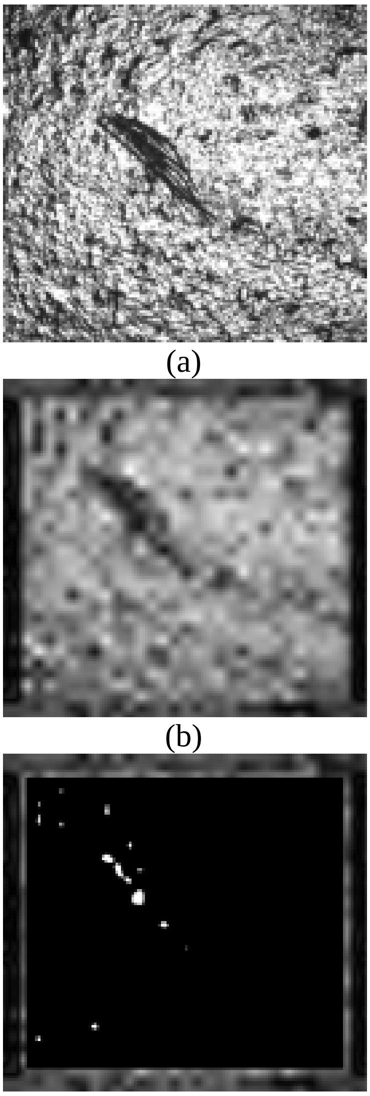

(a)

(b)

(c)

Figure 16. Detecting the defect in a cast surface: (a) a defective surface; (b) the reconstructed image; (c) the binarized result of (b).

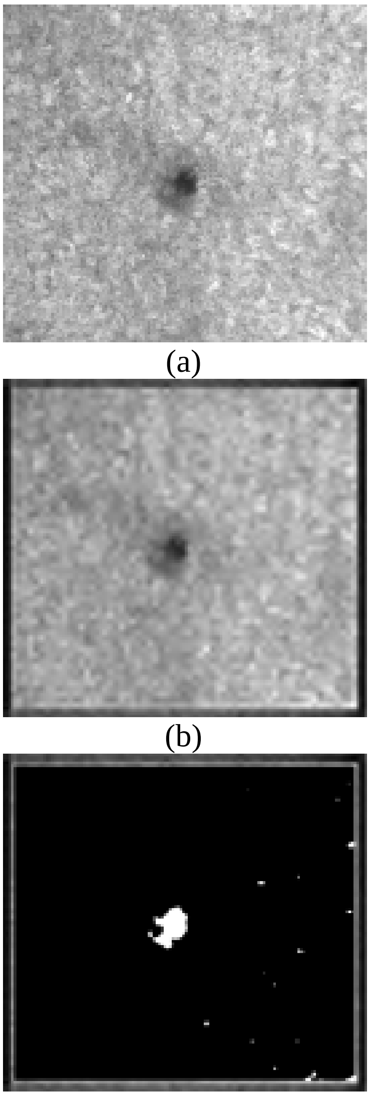

(a)

(b)

(c)

Figure 17. Detecting the defect in a wool surface: (a) a defective surface;(b) the reconstructed image; (c) the binarized result of (b).

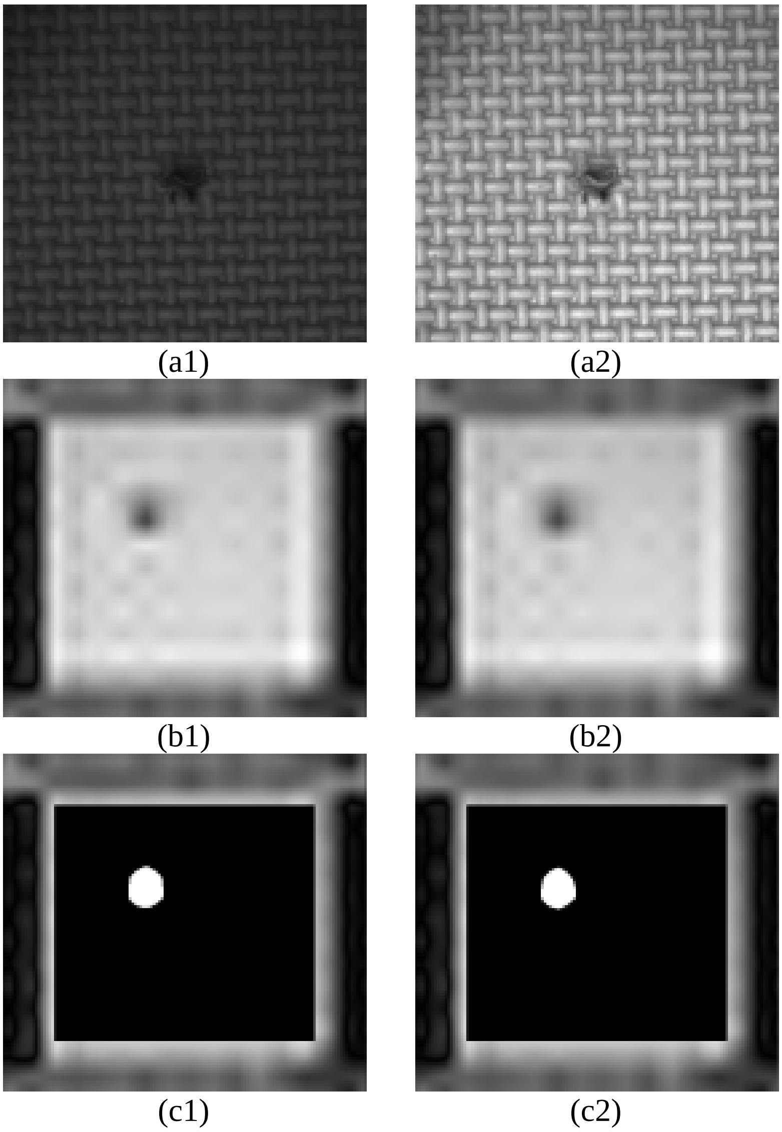

(a1) (a2)

(b1) (b2)

(c1) (c2)

Figure 18. (a1), (a2) The underexposed and overexposed images of the bamboo weave texture shown in Figure 14(a); (b1), (b2) the corresponding restored images; (c1), (c2) the resulting binary images of (b1) and (b2), respectively.

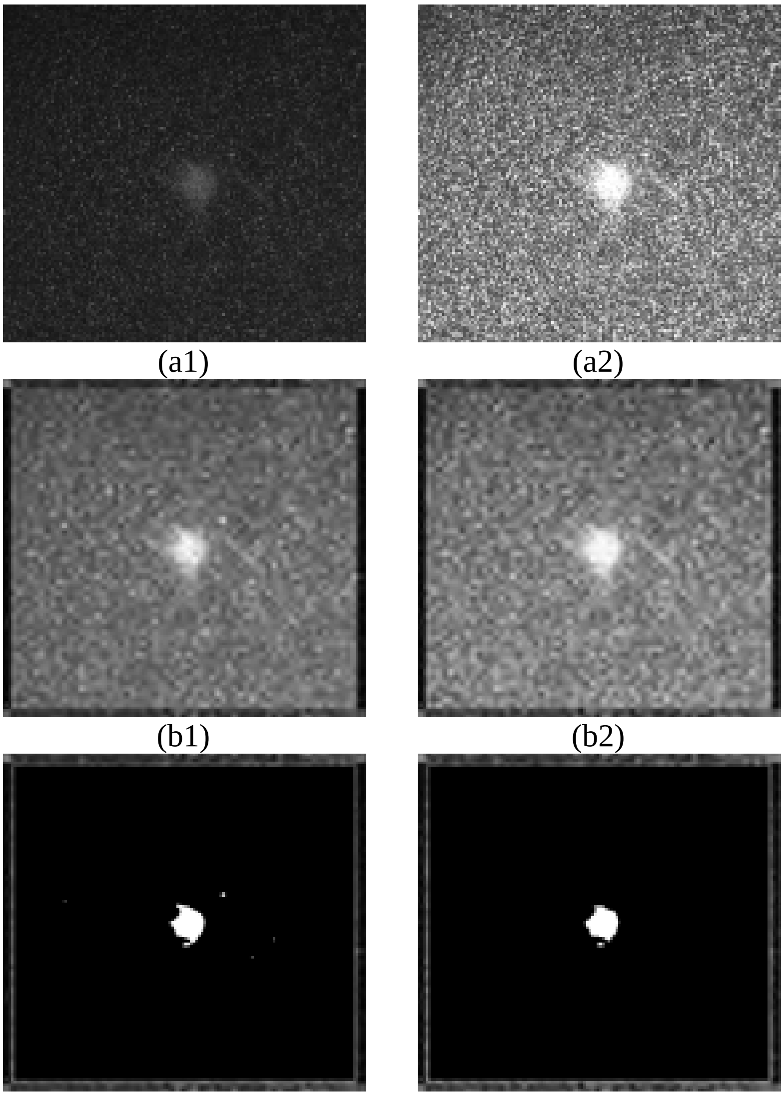

(a1) (a2)

(b1) (b2)

(c1) (c2)

Figure 19. (a1), (a2) The underexposed and overexposed images of the sandpaper texture shown in Figure 13(d); (b1), (b2) the corresponding restored images; (c1), (c2) the resulting binary images of (b1) and (b2), respectively.

Table 1. Normalized energies of four decomposed subimages at resolution level J=1, 2, 3: (a) statistics for Figure 5; (b) statistics for Figure 6; (c) statistics for Figure 7.

(a)

| Resolution level | Smooth subimage | Horizontal detail | Diagonal detail | Vertical detail |
|---|---|---|---|---|
| | $E_S$ | $E_H$ | $E_D$ | $E_V$ |
| J=1 | 0.992 | 4.961E-17 | 3.843E-19 | 7.687E-3 |
| J=2 | 0.980 | 1.022E-16 | 9.773E-19 | 1.954E-2 |
| J=3 | 0.953 | 1.693E-16 | 2.311E-18 | 4.623E-2 |

(b)

| Resolution level | Smooth subimage | Horizontal detail | Diagonal detail | Vertical detail |
|---|---|---|---|---|
| | $E_S$ | $E_H$ | $E_D$ | $E_V$ |
| J=1 | 0.992 | 4.332E-3 | 9.986E-4 | 2.776E-3 |
| J=2 | 0.982 | 8.407E-3 | 3.177E-3 | 6.319E-3 |
| J=3 | 0.974 | 1.156E-2 | 5.116E-3 | 9.008E-3 |

(c)

| Resolution level | Smooth subimage | Horizontal detail | Diagonal detail | Vertical detail |
|---|---|---|---|---|
| | $E_S$ | $E_H$ | $E_D$ | $E_V$ |
| J=1 | 0.998 | 1.110E-3 | 8.691E-5 | 4.192E-4 |
| J=2 | 0.992 | 3.278E-3 | 2.884E-3 | 1.818E-3 |
| J=3 | 0.984 | 6.765E-3 | 4.478E-3 | 4.001E-3 |

Table 2. The energy ratios $R_j$ for Figure 8.

| Resolution level j | $E_S = E_s^j / E$ | $D_j = (E_h^j + E_v^j + E_d^j) / E$ | $R_j = D_j / D_{j-1}$ |
|---|---|---|---|
| j=1 | 0.983 | 0.017 | - |
| j=2 | 0.943 | 0.040 | 2.383 |
| j=3 | 0.877 | 0.066 | 1.637 |
| j=4 | 0.792 | 0.085 | 1.284 |
| j=5 | 0.500 | 0.292 | 3.446 |

Table 3. Normalized energies of four decomposed subimages: (a) statistics for Figure 9(a); (b) statistics for Figure 10(a).

(a)

| Resolution level | Smooth subimage | Horizontal detail | Diagonal detail | Vertical detail |
|---|---|---|---|---|
| | $E_S$ | $E_H$ | $E_D$ | $E_V$ |
| J=1 | 0.995 | 1.092E-3 | 1.290E-4 | 3.100E-3 |
| J=2 | 0.977 | 2.990E-3 | 6.149E-4 | 1.627E-2 |
| J=3 | 0.940 | 5.956E-3 | 1.128E-3 | 5.274E-2 |

(b)

| Resolution level | Smooth subimage | Horizontal detail | Diagonal detail | Vertical detail |
|---|---|---|---|---|
| | $E_S$ | $E_H$ | $E_D$ | $E_V$ |
| J=1 | 0.996 | 2.435E-3 | 5.058E-4 | 4.830E-4 |
| J=2 | 0.984 | 1.340E-2 | 1.214E-3 | 1.167E-3 |
| J=3 | 0.942 | 4.933E-2 | 3.952E-3 | 3.919E-3 |

Table 4. Energy statistics for Figure 11(a): (a) normalized energies of four decomposed subimages; (b) energy ratio $R_j$.

(a)

| Resolution level | Smooth subimage | Horizontal detail | Diagonal detail | Vertical detail |
|---|---|---|---|---|
| | $E_S$ | $E_H$ | $E_D$ | $E_V$ |
| J=1 | 0.998 | 3.927E-4 | 1.261E-4 | 1.012E-3 |
| J=2 | 0.992 | 1.451E-3 | 7.839E-4 | 5.083E-3 |
| J=3 | 0.977 | 3.969E-3 | 2.279E-3 | 1.588E-2 |

(b)

| Resolution level j | $E_S = E_s^j / E$ | $D_j = (E_h^j + E_v^j + E_d^j) / E$ | $R_j = D_j / D_{j-1}$ |
|---|---|---|---|
| j=1 | 0.998 | 0.002 | - |
| j=2 | 0.992 | 0.006 | 3.779 |
| j=3 | 0.977 | 0.015 | 2.560 |
| j=4 | 0.956 | 0.021 | 1.478 |
| j=5 | 0.854 | 0.102 | 4.653 |

Table 5. Energy statistics for Figure 13(a): (a) normalized energies of four decomposed subimages; (b) energy ratio $R_j$ .

(a)

| Resolution level | Smooth subimage | Horizontal detail | Diagonal detail | Vertical detail |
|---|---|---|---|---|
| | $E_S$ | $E_H$ | $E_D$ | $E_V$ |
| J=1 | 0.975 | 1.264E-2 | 3.083E-3 | 9.330E-3 |
| J=2 | 0.930 | 3.251E-2 | 1.133E-2 | 2.556E-2 |
| J=3 | 0.892 | 4.840E-2 | 2.078E-2 | 3.831E-2 |

(b)

| Resolution level j | $E_S = E_s^j / E$ | $D_j = (E_h^j + E_v^j + E_d^j) / E$ | $R_j = D_j / D_{j-1}$ |
|---|---|---|---|
| j=1 | 0.975 | 0.025 | - |
| j=2 | 0.930 | 0.045 | 1.770 |
| j=3 | 0.892 | 0.038 | 0.858 |
| j=4 | 0.840 | 0.052 | 1.370 |
| j=5 | 0.589 | 0.251 | 4.807 |